metals

Article

The Effects of Cold Rolling and Annealing on the Microstructure Evolution of Ordered C-2000 Alloy during Metallic Wire Preparation

Liang Yuan [1,*], Faqiang Gou [1], Deqiang Sun [1], Zhiqiang Li [1] and Yunlong Xue [2]

[1] College of Bioresources Chemical and Materials Engineering, Shaanxi University of Science and Technology, Xi'an 710021, China
[2] School of Material Science & Engineering, Shaanxi University of Science and Technology, Xi'an 710021, China
* Correspondence: yuanliang@sust.edu.cn; Tel.: +86-29-86168070

Abstract: When using well-designed multiple-stage heavy-drawn processes, i.e., cold rolling, drawing and cluster drawing to fabricate a metallic wire or fiber in steps, cold rolling and annealing are critical steps due to their effect on the initial microstructure before the heavy-drawn process. Understanding the relationship between microstructure evolution and cold rolling followed by annealing is required for smoothly implementing the heavy-drawn process. In this work, the evolution behavior in terms of the microstructure during cold rolling followed by annealing was investigated in a novel C-2000 alloy that is a promising candidate material for the fabrication of high-performance metallicwire. The investigation encompassed parameters including the grain size, grain boundaries, recrystallization texture, and short-range ordered (SRO) structure. Results show that the grain size distribution of the cold-rolledC-2000 alloy followed by annealing at 900 °C is quite uneven. The low-angle grain boundaries induced by cold rolling are more frequently transformed into the $\Sigma3$ twin boundaries during recrystallization. At the initial stage of annealing at 900 °C after cold rolling, the contents of different texture components are significantly different, but the differences tend to decrease with the extension of the annealing time. In addition, cold rolling destroys SRO domains formed during solid solution water quenching, and the destruction of SRO affects the precipitation of the long-range ordered phase during annealing. Incoherent $\Sigma3_{ic}$ with curved grain boundaries play an important role in the recrystallization of nucleation sites in the process of static recrystallization by nucleation–growth.

Keywords: microstructure; texture component; ordered C-2000 alloy; cold rolling; annealing; short-range order (SRO) structure; incoherent $\Sigma3_{ic}$

check for updates

Citation: Yuan, L.; Gou, F.; Sun, D.; Li, Z.; Xue, Y. The Effects of Cold Rolling and Annealing on the Microstructure Evolution of Ordered C-2000 Alloy during Metallic Wire Preparation. *Metals* **2023**, *13*, 651. https://doi.org/10.3390/met13040651

Academic Editor: Gabriela Vincze

Received: 14 February 2023
Revised: 20 March 2023
Accepted: 23 March 2023
Published: 25 March 2023

1. Introduction

Metallic wires with an excellent combination of mechanical and corrosion resistance properties are highly desired for various engineering applications, such as heavy lift slings and offshore platform rigging [1,2]. At present, pearlitic steel wire is the most mature and widely used material [3]. However, the service environment for metallic wires is becoming increasingly complex and extreme, e.g., the coal filter made of metal wires or fibers has to withstand the erosion of high temperature complex atmosphere and the impact of the cyclic load in the service environment. Hence, it is important to use novel alloy instead of traditional pearlitic steel to develop high performance metallic wires that can safely serve in a variety of harsh environments.

It is well known that Ni–Cr–Mo alloys, especially the recently developed Hastelloy C-2000 alloy containing high concentrations of Cr and Mo, exhibit exceptional corrosion resistance under extreme exposure conditions [4]. The high corrosion resistance is generally attributed to their elemental composition and the passive behavior it induces [5]. A considerable amount of work was conducted in the past to evaluate the alloy's passive behavior [4–6]. In addition, the formation of long-range ordered (LRO) precipitates through the disordering–ordering transition can significantly improve the mechanical properties of the C-2000 alloy [7–10]. Therefore, exploring the strengthening mechanism in aged Ni–Cr–Mo has also attracted wide attention [11–15].

Since Ni–Cr–Mo alloys exhibit an excellent combination of corrosion resistance and mechanical properties (good strength–ductility), C-2000 alloy is a very promising candidate for the fabrication of high-performance metallic wires. A schematic diagram from the alloy bar to the wire and then to the fiber was shown in Figure 1. It is clear that plastic deformation (cold rolling) and heat treatment (annealing) are essential steps in the manufacture of metallic wires. Moreover, when the metallic wire is further transformed into a fiber using the multiple-stage heavy-drawn process, a series of plastic deformation and heat treatment steps are also involved, such as drawing, intermediate annealing, and cluster drawing. During cold rolling and annealing, the changes in the microstructure of the alloy, including the size and orientation of the grain, grain boundary characteristics, and texture components, will significantly affect the mechanical properties of the material. For example, the initial crystallographic orientation under dynamic plastic deformation affects the twinning tendency of Cu single crystals [16]. After two-step recrystallization annealing, a strong recrystallization cube texture formed in Ni–W alloy not only affects the mechanical properties of the alloy [17], but reduces the magnetization losses [17,18]. Undoubtedly, the changes in the microstructures during cold rolling and annealing will directly affect the implementation of the subsequent heavy-drawn process. In addition, the change in grain boundaries caused by the cold rolling followed by annealing needs to be carefully controlled, since the high percentage of $\Sigma 3$ grain boundaries limits the initiation of localized corrosion [19]. It was shown that increasing the fraction of the low energy Σ ($3 \leq \Sigma \leq 29$) coincidence site lattice (CSL) boundaries improves the cracking resistance [20] and corrosion resistance [21] of alloys. It was reported by Sakaguchi et al. [22] that the discontinuous groove along the asymmetric facet was completely disrupted by the coherent twin boundary at faceted $\Sigma 3$ grain boundaries.

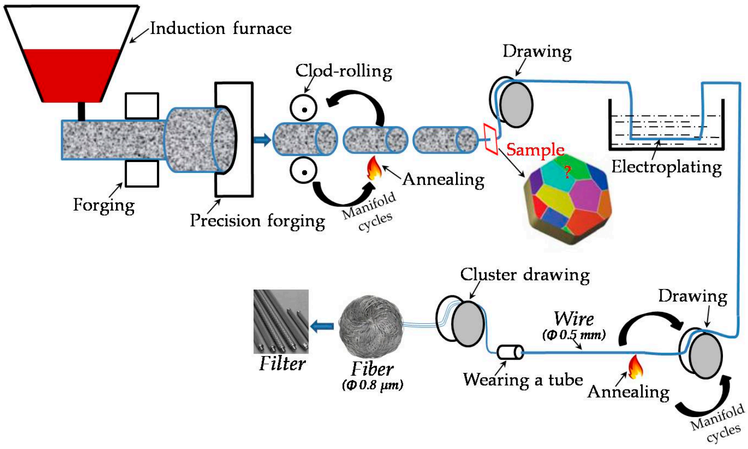

Figure 1. Schematic diagram from bar to wire and then to fiber.

Therefore, understanding the microstructure evolution of the C-2000 during cold rolling and annealing is critical for the successful preparation of high-performance metallic wires or fibers. However, until recently, the microstructure evolution of a novel C-2000 alloy after plastic deformation followed by annealing had not been systematically investigated, particularly the evolution of texture components, despite the fact that He et al. [23] focused on the evolution behavior of $\Sigma 3^n$n CSL boundaries in the C-2000 alloy during aging. On the other hand, it was reported [12] that soli-solution water quenching can induce the emergence of small-scale short-range order (SRO) domains in a Ni–Cr–Mo-based alloy, which will affect the precipitation behavior of the strengthening precipitates (LRO) during subsequent heat treatment. Currently, the study of the SRO domains mainly focuses on the characterization of their morphology and size by TEM [24]. Few people pay attention to the effect of plastic deformation on SRO domains. Until recently, it is not clear whether cold rolling affects SRO domains, which is actually very important for the microstructure evolution in the subsequent annealing process. The primary goal of this work is to thoroughly understand the effects of cold rolling and annealing treatment on the microstructure of the C-2000 alloy, as well as to reveal the evolution of various types of microstructures in the C-2000 alloy. Moreover, the evolution of the SRO domains after cold rolling was also studied.

2. Materials and Methods

A commercial C-2000 bar used in this study was received in a hot-rolled and annealed state by Haynes International Inc., Kokomo, IN, USA, and its chemical composition is given in Table 1. As shown in Figure 1, it is necessary to briefly describe the preparation process of metallic wires/fibers. The as-received alloy bar was cut into along piece using electrical discharge machining. The alloy rod was cold-rolled in steps along longitudinal direction through five passes. After the first rolling pass, the rod was preheated at 900 °C for 30 min; between all subsequent passes, reheating to 900 °C was performed for about 30 min. The cold-rolled rod was then cold-drawn to a smaller scale. The drawing speed was 4 m/min. After that, the wire was further cold-drawn through 10 passes. After every two passes, the cold-drawn wire was annealed at 900 °C for about 15 min, and the drawing speed was also 4 m/min. To remove the oxide coating from the surface, the wire was then simply polished. Finally, the wire was threaded through the tube, and then the metallic fiber with a diameter of 0.8 μm is obtained by cluster drawing. To study the role of cold rolling and annealing on the initial microstructure before it being heavy-drawn, a cylinder 50 (RD_1) ×50 (RD_2) ×10 (ED) mm^3 was cut from the C-2000 bar (where RD_1, RD_2, and ED are the two radial directions and the extrusion direction, respectively). A solid solution treatment was carried out in a tube furnace with continuous argon flow at 1150 °C for 30 min, followed by cold water quenching. The quenched sample was then cold-rolled with a reduction of 50% with several passes. Then, the cold-rolled sample received annealing treatment at 900 °C for 15 min and 120 min, respectively. To illustrate the effect of the cold rolling deformation on the SRO domains, the microstructure of two kinds of samples treated by the following two processes was also characterized by transmission electron microscopy (TEM): (i) the quenched sample was subjected to 50% cold-rolled deformation and then isothermal aging and (ii) the quenched sample was directly isothermally aged.

Table 1. Chemical composition of as-received C-2000 alloy bar (wt.%).

Cr	Mo	Cu	Fe	Al	Mn	Co	Si	P	S	C	Ni
22.66	15.8	1.53	0.75	0.24	0.23	0.20	0.02	0.003	0.001	0.001	Bal.

The microstructure analyses were carried out by a field emission scanning electron microscope (SEM, JSM-7900F, JEOL Inc., Tokyo, Japan) equipped with electron backscatter diffraction (EBSD, EDAX HikariSuper, AMETEK Inc., Mahwah, NJ, USA) FEI Inspect F7900 field emission gun scanning electron microscope operating at 20 kV with an s step size of 0.6 μm. Specimens for EBSD were electro-polished by a direct current with a solution consisting of 5 vol% perchloric acid + 95 vol% alcohol at 35 V and −20 °C for 80 s. Random low-angle grain boundaries (LAGBs), medium-angle grain boundaries (MAGBs), and high-angle grain boundaries (HAGBs) were defined as boundaries having misorientation angles θ in a range of 2–5°, 5–15°, and $\theta \geq 15°$, respectively. The Brandon criterion (i.e., $\Delta\theta_{max} \leq 15°\Sigma^{-1/2}$, where $\Delta\theta_{max}$ is the maximum deviation of misorientation angle) was used to assess the low Σ ($3 \leq \Sigma \leq 29$) coincidence site lattice (CSL) boundaries. The threshold value of texture components of samples calculated by using the CHANNEL 5 software (HKL Channel 5.0, Oxford Instrument, Oxford, UK) is set to 15°. To eliminate spurious boundaries caused by orientation noise, the boundary misorientation of less than

2° was cutoff while the maximum misorientation angle (from the center) along the axis parallel to this symmetry axis (m-3m) is limited to 60° according to the Hough-based EBSD angular resolution. The CHANNEL5 software developed by HKL Inc. (Oxford, UK), was used to analyze the EBSD data.The thin foil specimen for TEM was first mechanically polished to a thickness of ~50 μm. Then, electropolishing was performed with a double-jet electropolishing device using an electrolyte comprising 20% perchloric acid and 80% ethanol by volume under a temperature of −25 °C. TEM characterizations were carried out by transmission electron microscopy (TEM, FEI Tecnai 30, Philips-FEI, Amsterdam, The Netherlands) at an accelerating voltage of 200 kV.

3. Results and Discussion

3.1. Microstructure of the As-Received Sample

The initial microstructure of the as-received C-2000 bar obtained by the EBSD technique is shown in Figure 2. It can be seen from Figure 2a that the microstructure consists of all single equiaxed γ grains (aspect ratio ≈ 1.768) with a face-centered structure (FCC). As shown in Figure 2c, although the average grain size of the as-received C-2000 bar is approximately 10.13 μm, its histogram displays inhomogeneity ranging from 1.5 μm to 48.5 μm. The fraction of coarse grains (mean diameter higher than 11 μm) and fine grains (less than 11 μm) is about 17% and 83%, respectively. A large number of lamella-like straight structures (Figure 2b) are observed within the grains, which corresponds well to annealing twins due to the low stacking fault energy (SFE) of the experimental C-2000 alloy with an FCC structure [23]. Although pure Ni has a high SFE of ~150 mJ/m^2, it has been documented that alloying elements such as Cr, Mo, Cu, and Al can substantially lower the value of SFE. Clearly, a distinct peak at 55–60° shared a strong <111> rotation axis, as shown in Figure 2d and the corresponding inset, respectively. It should be noted that the Σ3 twin boundaries were regarded as grain boundaries in the above grain size measurements.

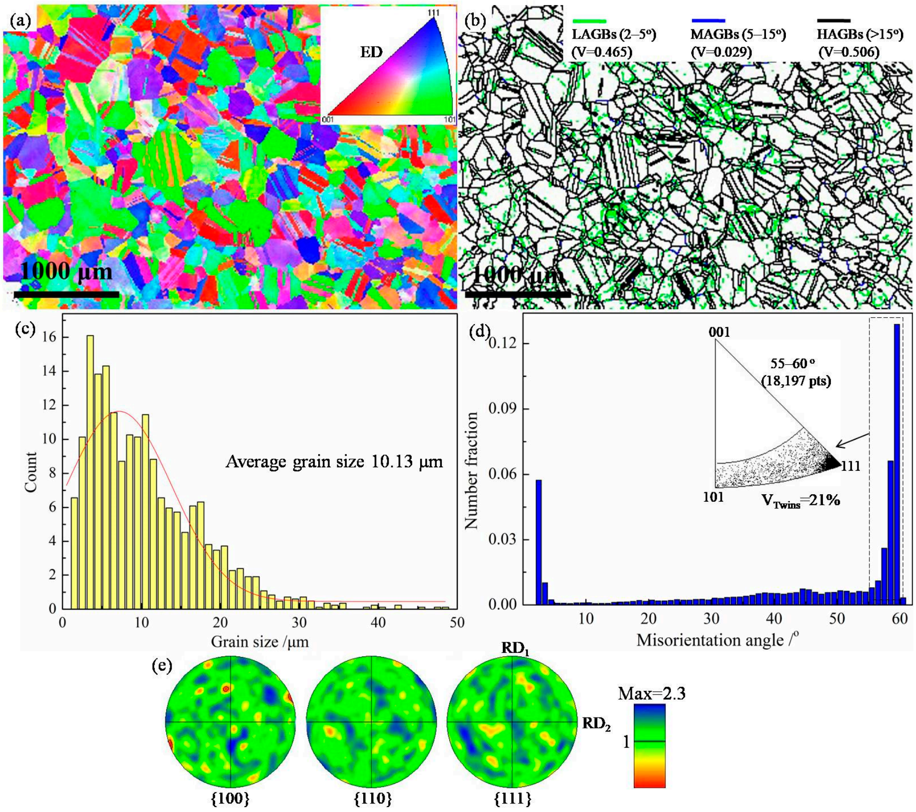

Figure 2. Microstructure of the as-received bar under EBSD measurement: (**a**) inverse pole figure image; (**b**) grain boundary map; (**c**) grain size distribution; (**d**) histogram of the misorientation angle and the inset showing distribution diagram of angular axis of Σ3 twin; and (**e**) pole figure (PF).

In addition, some of the grains are filled with LAGBs in Figure 2b, resulting from the rearrangement and movement of dislocations. The fractions of HAGBs and MAGBs are 0.506 and 0.029, respectively, which suggests that some defects formed during extrusion followed by annealing were almost negligible. Moreover, the result from the PF in Figure 2e shows that the microstructures of the as-received C-2000 bar possess a random texture, i.e., no preferential orientations for the polycrystalline C-2000 alloy.

3.2. Texture Components of the As-Received C-2000 Bar

Generally, it is possible in certain cases to minimize or develop the desired texture, but it is almost impossible to produce true randomness in the microstructure. In other words, either more or fewer texture components or preferred orientations exist in the polycrystalline material [17]. More importantly, a detailed knowledge of the texture of a metallurgical specimen can help deduce its mechanical and thermal histories to a great extent. Meanwhile, the dependence of the mechanical properties of materials during processing on texture components influences not only the deformation mechanisms but the kinetics of different types of transformation too. Based on both the characteristics and the importance of the aforementioned texture, the texture components of the as-received C-2000 bar were shown in Figure 3. Compared with the ideal texture, the threshold value of texture components of samples calculated by using the CHANNEL5 software is set to 15°. By comparing texture component maps (Figure 3a,b) combined with statistics of texture components (Figure 3c), it can be observed that the distribution of the plate texture is uniform and has a relatively low fraction. Meanwhile, the volume fraction of the brass texture with the highest proportion is only 6.12% (Figure 3c). In contrast, the volume fraction of the fiber texture increased to more than 11%, and the fraction of <110> fiber texture went up to about 24.6%.

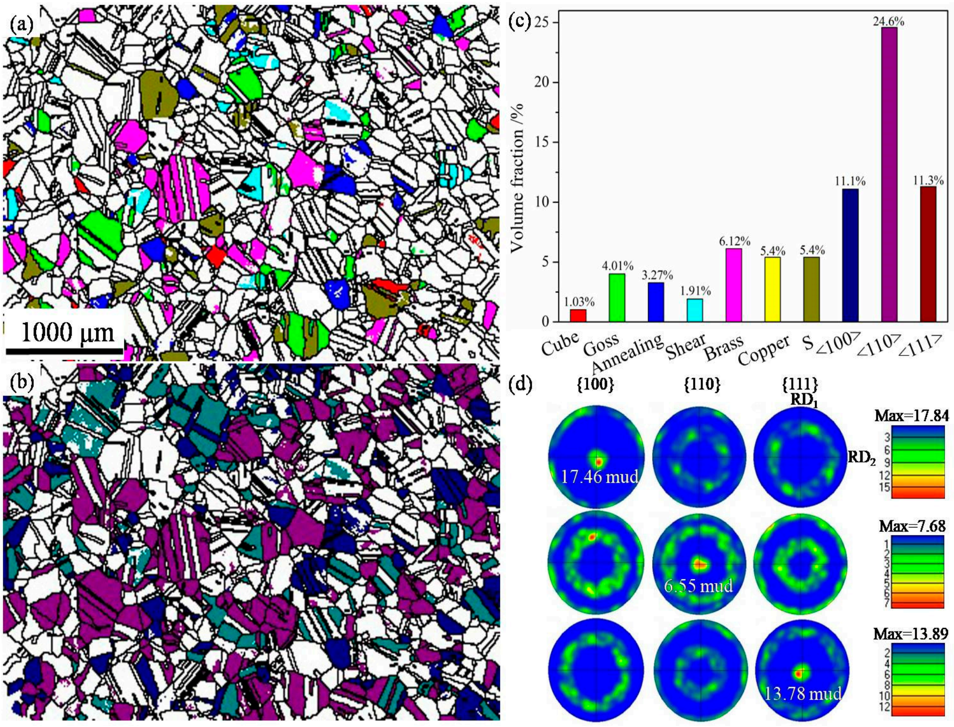

Figure 3. Characterization of the texture of the as-received sample: (**a**,**b**) texture components map; (**c**) statistics of texture; and (**d**) pole figure of fiber texture.

3.3. Microstructure of the Annealed Samples

Figure 4 shows IPF images and the corresponding histograms of the grain size distribution of the annealed sample. The microstructure comprising of of a few coarse grains surrounded by a large number of fine grains was observed in the annealed sample, as shown in Figure 4a,b. Although the grain size distribution of the annealed sample still displays an obvious peak for the fine grain size compared to that of the as-received C-2000 bar although there is a significant drop in the average grain size. The grain size decreased from approximately 10.13 µm (Figure 2c) as-received to an annealed sample of about 6 µm (Figure 4c,d). The appearance of abundant fine grains combined with a few coarse grains indicates that recrystallization is taking place under the current annealing conditions. It is well known that recrystallization in metals and alloys is a process in which the coarse grains with serious distortion are gradually swallowed by the new fine grains without distortion, resulting in a sharp decrease in overall grain size.

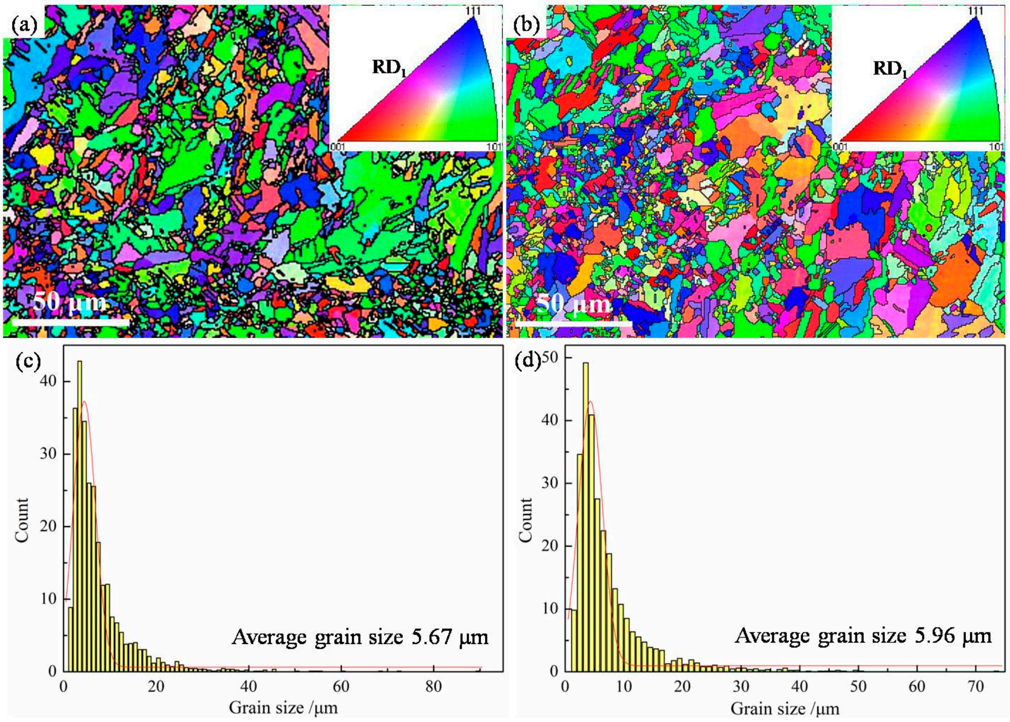

Figure 4. Microstructure of samples after different annealing times and the corresponding distribution of grain size: (**a**,**b**) IPF images; (**c**,**d**) histograms of grain size distribution; (**a**,**c**) annealing at 900 °C for 15 min; and (**b**,**d**) annealing at 900 °C for 120 min.

Figure 5 illustrates the grain boundary (GB) maps and their corresponding histogram of the misorientation angle of both cold-rolled and annealed samples. In these GBs maps, the black and green lines represent the HAGBs and LAGBs, respectively. After cold rolling, LAGBs with high densities were observed within grains, as shown in Figure 5a. Meanwhile, the distribution of the misorientation angle displays bimodal characteristics (Figure 5b), i.e., the peak occurs at 2–5° and 55–60°, respectively. After short-annealing at 900 °C for 15 min, the content of LAGBs reduced remarkably, as seen in Figure 5c. Compared with the characteristic misorientation angle of the cold-rolled sample, the misorientation angle distribution for annealed samples tends to range from 2–5° (Figure 2d) to 38–40° (Figure 5d,f). Furthermore, large amounts of bulging HAGBs are observed in annealed samples after annealing at 900 °C (Figure 5c,e), which is an indication of grain boundary sliding induced by deformation strain. It was reported that the serrated HAGBs, through grain boundary bulging, can usually become the potential nucleation sites of the recrystallization [25].

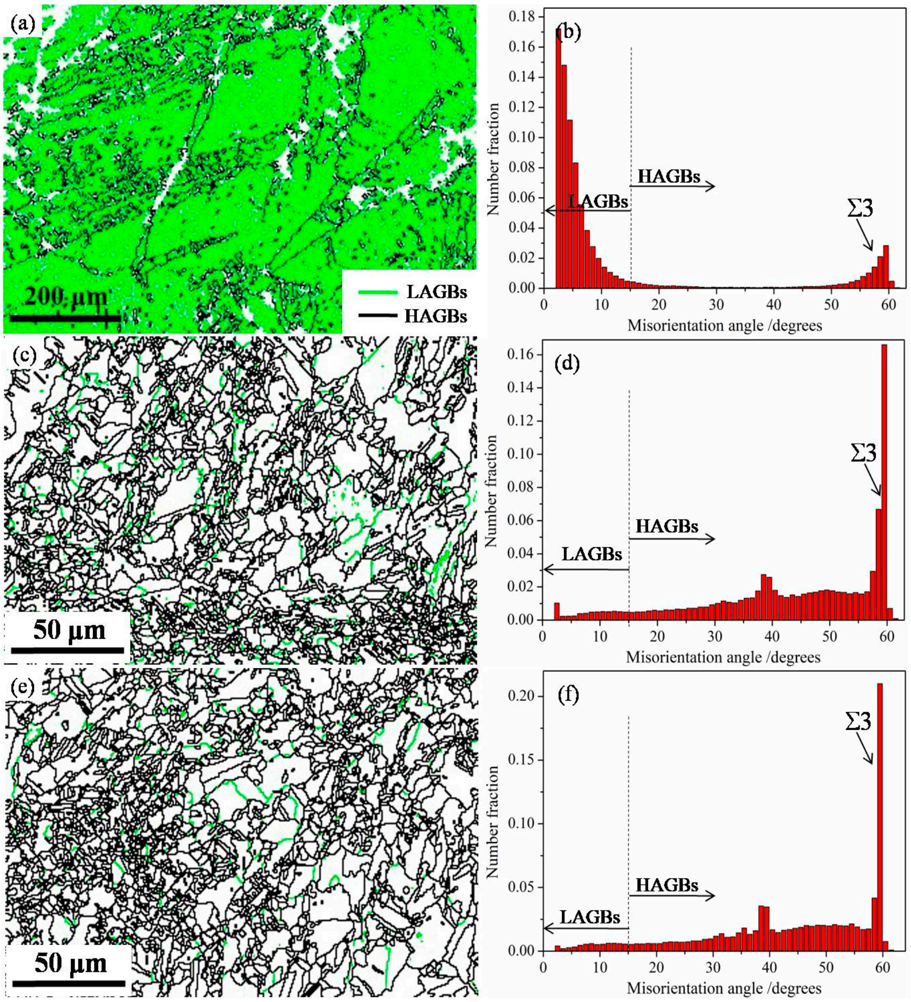

Figure 5. Evolution of grain boundary for different samples: (**a**,**c**,**e**) grain boundary map; (**b**,**d**,**f**) the corresponding misorientation angle; (**a**,**b**) deformed sample; (**c**,**d**) annealed sample at 900 °C for 15 min; and (**e**,**f**) annealed sample at 900 °C for 120 min.

The appearance of LAGBs with a high density during cold rolling is attributed to the proliferation of dislocations due to the continued trapping of newly created mobile dislocations by existing dislocations and their incorporation into the various microstructural features that are characteristic of the deformed state. The cold-rolled sample is subsequently heated to a high temperature of 900 °C, i.e., annealing treatment thermally activated processes such as solid state diffusion provide mechanisms whereby the defects raised during deformation may be removed or arranged in configurations requiring less energy. As a result, the number of HAGBs increases rapidly, while that of LAGBs decreases sharply with the formation of the recrystallized grains, because the recrystallization occurs when new dislocation-free grains are formed within the deformed or recovered structure by the migration of HAGBs.

It is well known that kernel average misorientation (KAM) or local misorientation maps in EBSD technology can be used to describe the deformation degree of the grain. The green color in the KAM map can be regarded as dislocation caused by lattice distortion during deformation. Hence, the evolution of grain boundaries during cold rolling followed by annealing can also be well confirmed by the KAM map. As shown in Figure 6, the dislocation density for the annealed sample decreases sharply, and a few of the dislocations distribute sporadically in un-recrystallization grains. Using the Formulas (1) and (2) under the KAM method [26,27], the geometrically necessary dislocations (*GND*) density is 6.95×10^{13} m^{-2} (cold-rolled), 1.86×10^{13} m^{-2} (annealing for 15 min), and 1.54×10^{13} m^{-2}

(annealing for 120 min), respectively. The decreasing trend of *GND* density after cold rolling followed by annealing is consistent with the variation of LAGBs in Figure 5.

$$\Delta\theta_{\mathrm{i}} = \frac{1}{n}\sum_{j=1}^{n}\left|\theta_j^{sur} - \theta_i\right| \tag{1}$$

$$\rho^{GND} = \frac{2\Delta\theta_i}{ub} \tag{2}$$

where $\Delta\theta_i$ represents the local misorientation; θ_i represents the local misorientation at the point "i" and θ_i^{sur} is the mirorientation at its neighboring point. ρ^{GND} is *GND* density at the point of interest; u is the unit length of the point; b is the Burgers vector.

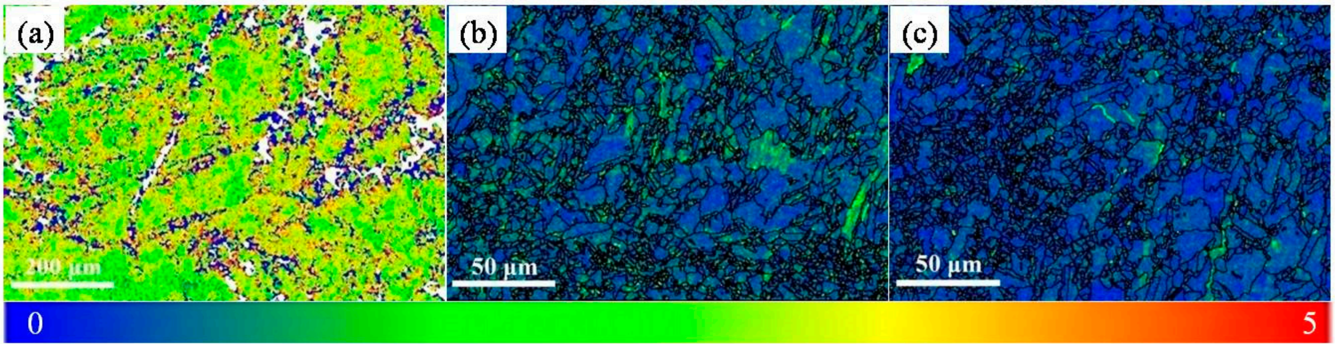

Figure 6. KAM maps of different samples: (**a**) cold rolling; (**b**) annealing for 15 min; and (**c**) annealing for 120 min.

3.4. Evolution of Texture Components during Annealing

It is known that the original deformed sub-structures are replaced by a large number of small strain-free grains when the deformed material is subsequently recrystallized [28]. Since static recrystallization involves the nucleation of new grains and their growth through the migration of HAGBs, this may cause characteristic changes in the crystallographic orientation or texture. Depending on the material itself and the deformation conditions, the recrystallization texture either looks identical to the deformation texture or very different from the deformation texture. Sometimes, a deformation texture may also transform into a rather random and chaotic recrystallization texture. Sarma et al. reported [18] that a strong recrystallization cube texture was obtained when the cold-rolledNi-5at.%W alloy containing Cu {112}<111> and S {123}<634> was annealed. Therefore, it is worth studying the change of different texture components during recrystallization.

To illustrate the evolution of texture components, the histogram of the volume fraction of texture components is shown in Figure 7. As shown in Figure 7a, after annealing at 900 °C for 15 min, the volume fraction of the annealing texture increased from 3.27% in the as-received C-2000 bar to 6.27% in the annealed sample, and that of the brass texture decreased from 6.12% to 2.13%. Although other types of textures all show a change of rising and falling, the fluctuation range is not large. The volume fraction of each component in the plate texture tends to be more uniform when the annealing time is further extended to 120 min, although a short annealing of 15 min does not have a great influence on the volume content of the three kinds of fiber texture, as shown in Figure 7b. The volume distribution of the three kinds of fiber texture tends to be homogeneous when the recrystallization is completed with an increase inthe annealing time.

FCC metals and alloys are known to exhibit two different types of rolling textures: (i) α-brass or alloy type in materials of low SFE and (ii) copper or pure metal type in materials of medium and high SFE. A strong brass (B) {110}<112> and a minor Goss (G) {110}<001> component are present in in the α-brass or alloy type texture. In the copper or pure metal-type texture, the copper (Cu) {112}<111>, the S {123}<634>, and the B component are present in nearly equal proportions. The origin of the recrystallization cube texture in FCC alloys with high SFE lies in the deformation texture where the pure metal-type Cu and S orientations are predominant [29]. Reasonably, the cube texture with a low volume content (2.62%) and the B texture with a high volume content (5.49%) could be obtained in the annealed sample due to the experimental alloy with low SFE, as shown in Figure 7a. Moreover, a low rolling reduction of 50% may also hinder the formation of the cube texture in the final annealing due to the nucleation of random orientations in the B textured grains. Despite the low volume content of the cube texture, a gradual upward trend of the cube texture is observed with increasing annealing time, which is attributed to two factors: (i) the cube orientation partially recovers during low annealing temperatures of 900 °C and (ii) the lower activation energy for sub-grain growth at a low annealing temperature of 900 °C is also beneficial for the growth of the cube orientation.

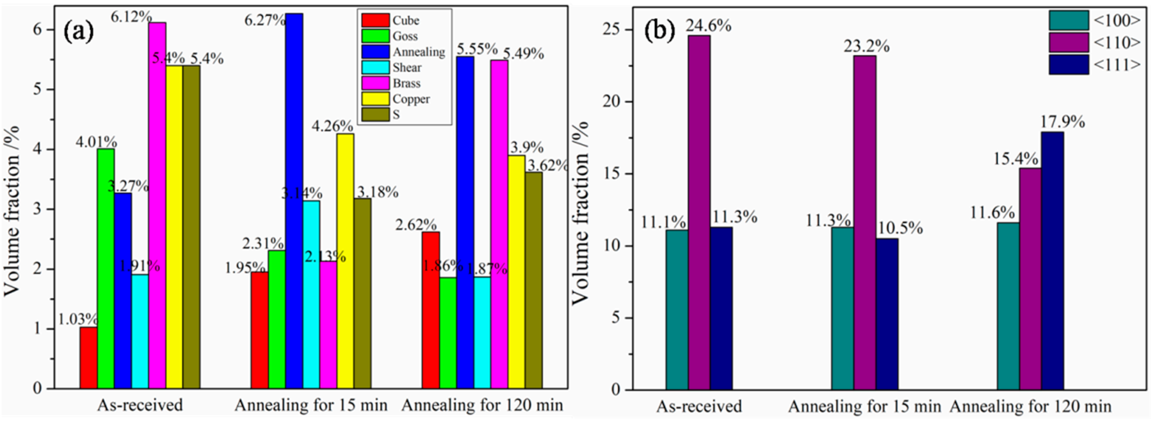

Figure 7. Texture components of the recrystallized grains: (**a**) plate texture and (**b**) fiber texture.

It was established, based on analysis of data from a number of alloy systems, that the dislocation's planar slip correlates more with the degree of SRO structure than with small values for the ratio of SFE and shear modulus [18]. The presence of the SRO structure affects the deformation behavior of the alloy and the precipitation of the LRO phase during aging.

Figure 8a shows the presence of SRO in the quenched sample without plastic deformation as revealed by the appearance of the weak reflections at the characteristic {1½0} positions (marked by a white arrow) in the SAED pattern along the $[001]_{\text{matrix}}$ zone axis. In contrast, SRO-free characteristic spots were observed (Figure 8f) in the SAED pattern along the $[001]_{\text{matrix}}$ when the cold rolling deformation is applied to the quenched sample. As a result, the solid solution sample with and without deformation exhibits some tangling of dislocation (Figure 8e) and spherical particle precipitates (Figure 8b), respectively. It can be seen that spherical particle precipitates are uniformly dispersed in the alloy matrix, the average size of which is determined to be about 21 nm (Figure 8b) by the software program Image J and its volume fraction is calculated to be approximately 4.8% by a formula used by Lu et al. [30]. The SAED along [112] (inset in Figure 8b) indicates that the spherical particle precipitates are LRO with a Pt_2Mo-type structure. The SRO domain is unable to restore order when dislocation moving through the lattice destroys the SRO structure due to lattice ordering extending for only a short distance [31]. If the cold-rolled sample is subsequently heated to a high temperature (annealed), it leads to recrystallization involving the removal of dislocation defects and its rearrangement in configurations of lower energy. The dislocation slip rather than twinning (Figure 8c,d) becomes the dominant deformation mode due to the disappearance of the SRO after plastic deformation. When the dislocation slip is the main plastic deformation mode, it is equivalent to the alloy being in a high SFE state. As a result, the copper (Cu) {112}<111>, the S {123}<634>, and the B component are present in nearly equal proportions. Therefore, the multiple textures containing the S, Cu, and G-type textures all exit in the annealed sample. In addition, the nuclei are more randomly oriented with an increased annealing time. Hence, the content of multiple textures tends to be homogeneous in the annealed sample after annealing for 120 min, which is consistent with the result reported by Onuki et al. [32] that the cold rolling followed by annealing results in a nearly random distribution of crystal orientations in Fe-3wt.% Si alloy.

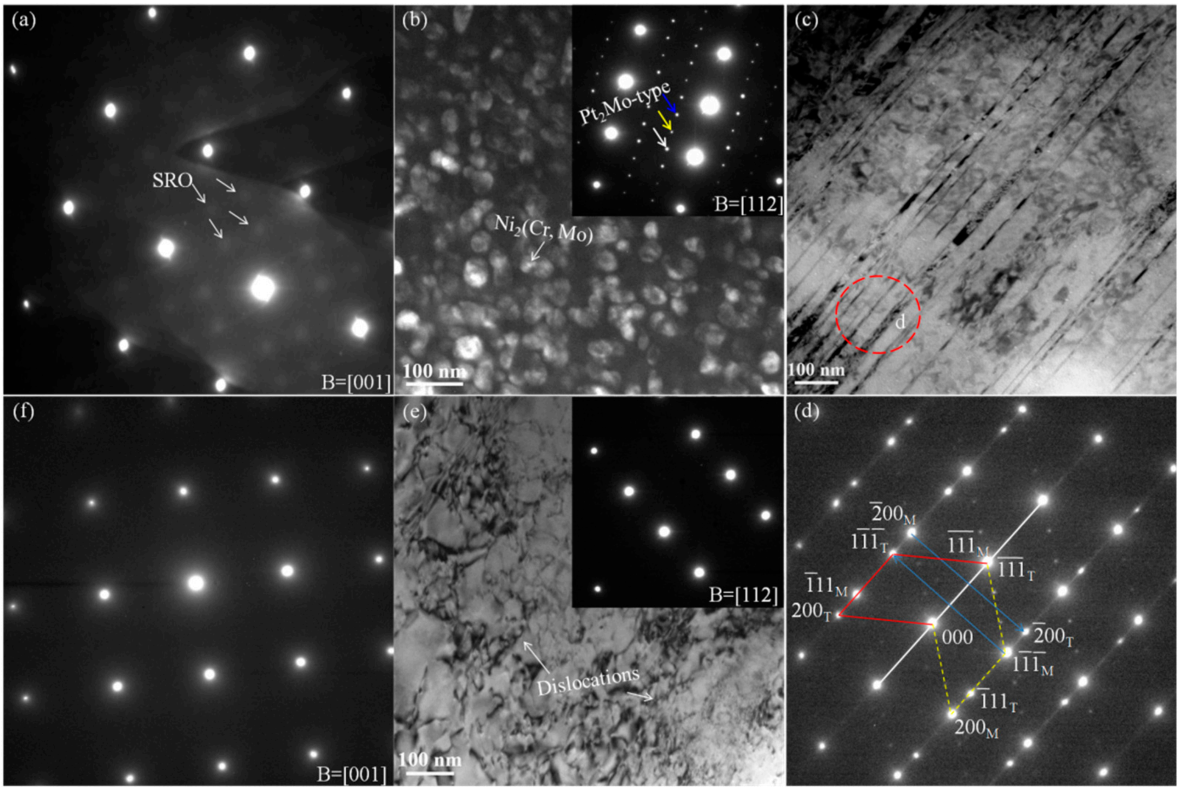

Figure 8. Effect of deformation on the microstructure of C2000 alloy: (**a**) SAED pattern along $[001]_{\mathrm{matrix}}$ of quenched sample; (**b**) DF image of sample after quenching followed by aging, and the inset showing SAED pattern along $[112]_{\mathrm{matrix}}$; (**c**) BF image of the aged sample during deformation; (**d**) SAED pattern taken from regions indicated by dotted circles in (**c**); (**e**) BF image sample after quenching followed by cold rolling of 50%, and the inset showing SAED along $[112]_{\mathrm{matrix}}$; and (**f**) SAED pattern along $[001]_{\mathrm{matrix}}$ after quenching, cold rolling of 50%, and aging.

After a short annealing of 15 min, as shown in Figure 9a, the orientation of the not recrystallized grains is preferred, among which the green color with <001> is more prominent. In contrast, the color of recrystallized grains in the inverse pole figure (IPF) image displays an untidy pattern, indicating that their orientation is random (Figure 9b). As the annealing time increases from 15 to 120 min, both not recrystallized and recrystallized grains exhibit a random orientation (Figure 9e,f).

To intuitively reveal the distribution of the recrystallized and not recrystallized grains, the scattering diagram of IPF is also shown in Figure 9. The concentration of green area in Figure 9d is less than that in Figure 9c, and the green recrystallized grains are projected in the <001> and <111>, indicating that the orientation of recrystallized grains is more random. However, the projection of green grains for the not recrystallized (Figure 9g) and recrystallized grains (Figure 9h) is more diffuse, implying their orientation is random. After short annealing, the grains not recrystallized still retain the structural characteristics of deformed grains, namely, the preferred orientation of the deformed grains will be inherited in the short-annealed samples. With the increase in annealing time, the crystallographic orientation of the not recrystallized grains will also change due to dislocation slip and grain rotation, leading to the weakening of the preferential orientation.

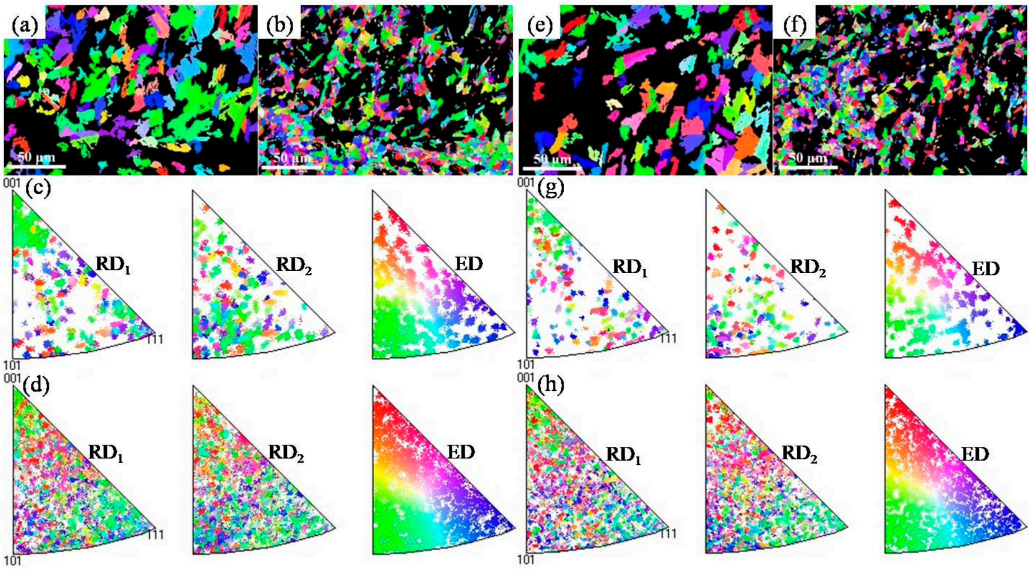

Figure 9. Orientation distribution of both un-recrystallized grains and recrystallized grains after different annealing times: (**a**,**e**) IPF image and (**c**,**g**) the corresponding IPF of un-recrystallized grains; (**b**,**f**) IPF image and (**d**,**h**) the corresponding IPF of recrystallized grains; (**a**–**d**) annealing for 15 min at 900 °C; and (**e**–**h**) annealing for 120 min at 900 °C.

3.5. Nucleation Mechanism of the Annealed C-2000 Alloy during Recrystallization

At present, four principal models of nucleation have been developed: (I) strain-induced boundary migration (SIBM), (II) twin nucleation, (III) dislocation plug area nucleation, and (IV) sub-grain growth. The SIBM mechanism is attributed to the difference in dislocation density or storage energy on both sides of HAGBs due to non-uniform plastic deformation. Regions with low dislocation density are arched into nearby grains with a higher dislocation density to form a bulge with a very low strain, which becomes the nucleation site of recrystallization. The KAM map from Figure 6b shows a certain difference in dislocation density that exists on both sides of HAGBs, which happens to be a condition for running the SIBM mechanism. Compared to severe plastic deformation (SPD), the cold rolling applied in this study produces a small amount of plastic deformation, which prompts the SIBM mechanism to become more energetic. Furthermore, due to the high dislocation density, the deformation dislocation plug area can act as a recrystallization nucleation site.

It was reported [33] that the dislocation in the cell wall may cause the motion of some Shockley partial dislocations to extend to the {111} plane of the adjacent cell structure, and then twin orientation will form when the Shockley partial dislocation sweeps in the corresponding cell structure. However, the 60°/<111> twin relationship with surrounding grains will be lost when the twin structure encounters other sub-structures, which results in the appearance of HAGBs with a high mobility. It should be mentioned [34] that the energies of Σ3 twin boundaries obey the following sequence: incoherent twin boundaries $\Sigma3_{ic}$ (0.1–0.6 Jm^{-2}) >coherent twin boundaries $\Sigma3_c$ (0.01 Jm^{-2}). It is reasonable to speculate, on the basis of Davies et al. [34], that the $\Sigma3_{ic}$ may be the main nucleation site of recrystallization.

An example of identifying a Σ3 twin boundary containing both $\Sigma3_c$ and $\Sigma3_{ic}$ twin boundaries regarded as nucleation sites of recrystallization by the single-section trace analysis is shown in Figure 10. As illustrated in Figure 10a, the serrated boundary among grain 1, grain 2, and grain 3 can be divided into three segments, and the trace normal parameters of the three segments are labeled $\vec{N}_1$, $\vec{N}_2$, and $\vec{N}_3$. It can be seen from the {111} pole figure (Figure 10b) of the three grains that the coincident pointsP_1, P_2, and P_3 are not located in the area of the normal trace. Therefore, it can be reasoned that the plane of boundary A differs from {111}, and boundary A is not a coherent twin boundary. However, it is found using the same method that the coincident point P_4 lies in the area corresponding to $\vec{N}_4$, which means the grain boundary plane is {111} and boundary B is confirmed to be coherent (Figure 10c). Based on the viewpoint [35] that straight and curved twin boundaries are classified as coherent and incoherent, respectively, it could be proposed that $\Sigma3_{ic}$ is the primary nucleation site of recrystallization due to abundant twin boundaries with a curved morphology within grains.

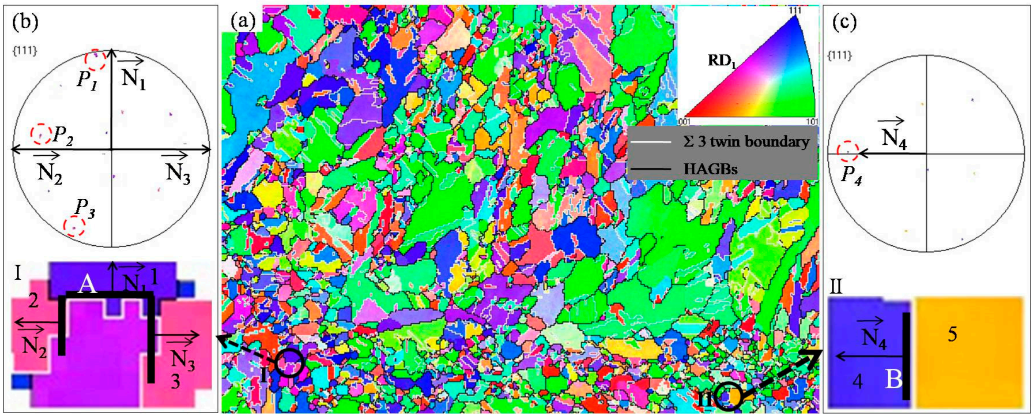

Figure 10. Identity of incoherent $\Sigma3_{ic}$ and coherent $\Sigma3_{c}$ during recrystallization nucleation: (**a**) IPF maps superimposed by both Σ3 twin boundaries and HAGBs; (**b**) local area magnification of area I in (**a**) and corresponding {111} pole figure; and (**c**) local area magnification of area II in (**a**) and corresponding {111} pole figure. Five grains with different orientation is marked with numbers 1–3 in area I and numbers 4, 5 in area II.

4. Conclusions

The grain size distribution of the cold-rolledC-2000 alloy followed by annealing at 900 °C is quite uneven, i.e., comprising a little coarse grain (~40 µm) surrounded by abundant fine grain (~6 µm). During recrystallization, the low-angle grain boundaries induced by cold rolling are more frequently transformed into the Σ3 twin boundaries.

At the initial stage of annealing at 900 °C after cold rolling, the contents of different texture components are significantly different, but the differences tend to decrease with the extension of the annealing time.

The cold rolling process destroys the SRO domains formed during solid solution water quenching. The destruction of SRO domains affects the precipitation behavior of LRO precipitates in the subsequent aging process and thus affects the deformation mode of the alloy. The incoherent $\Sigma3_{ic}$ with curved grain boundaries plays an important role in the process of selecting nucleation sites for recrystallization during static recrystallization with nucleation–growth as a mechanism.

Author Contributions: Writing—review and editing, funding acquisition, L.Y.; investigation, F.G.; formal analysis, D.S.; data curation, Z.L.; methodology, funding, Y.X. All authors have read and agreed to the published version of the manuscript.

Funding: This work was financially supported by The Natural Science Foundation of Shaanxi Province (No. 2022JM-196 (Liang Yuan), 2022GY-394 (Yunlong Xue)); The National Natural Science Foundation of China (No. 51701110, (Liang Yuan));The State Key Laboratory of Solidification Processing in NWPU (No. SKLSP201731 (Liang Yuan)); and The Shaanxi Key Laboratory of Green Preparation and Functionalization for Inorganic Materials (No. 202005 (Yunlong Xue)).

Institutional Review Board Statement: Not applicable.

Informed Consent Statement: Not applicable.

Data Availability Statement: Not applicable.

Conflicts of Interest: The authors declare no conflict of interest.

References

1. Borchers, C.; Kirchheim, R. Cold-drawn pearlitic steel wires. *Prog. Mater. Sci.* **2016**, *82*, 405–444. [CrossRef]
2. Zhang, X.; Godfrey, A.; Huang, X.; Hansen, N.; Liu, Q. Microstructure and strengthening mechanisms in cold-drawn pearlitic steel wire. *Acta Mater.* **2011**, *59*, 3422–3430. [CrossRef]
3. Zhang, X.; Hansen, N.; Godfrey, A.; Huang, X. Dislocation-based plasticity and strengthening mechanisms in sub-20 nm lamellar structures in pearlitic steel wire. *Acta Mater.* **2016**, *114*, 176–183. [CrossRef]
4. Zhang, X.R.; Zagidulin, D.; Shoesmith, D.W. Characterization of film properties on the Ni-Cr-Mo alloy C-2000. *Electrochim. Acta* **2013**, *89*, 814–822. [CrossRef]
5. Gray, J.J.; El Dasher, B.S.; Orme, C.A. Competitive effects of metal dissolution and passivation modulated by surface structure: Anafm and ebsd study of the corrosion of alloy 22. *Surf. Sci.* **2006**, *600*, 2488–2494. [CrossRef]
6. Mishra, A.K.; Ramamurthy, S.; Biesinger, M.; Shoesmith, D.W. The activation/depassivation of nickel-chromium-molybdenum alloys in bicarbonate solution: Part I. *Electrochim. Acta.* **2013**, *100*, 118–124. [CrossRef]
7. Li, X.M.; Bai, J.W.; Liu, P.P.; Zhu, Y.M.; Xie, X.S.; Zhan, Q. Coherent Ni_2(Cr, Mo) precipitates in Ni-21Cr-17Mo superalloy. *J. Alloys Compd.* **2013**, *559*, 81–86. [CrossRef]
8. Yuan, L.; Hu, R.; Li, J.S.; Zhang, X.Q.; Yang, Y.A. Portevin-Le Chatelier effect in a Ni-Cr-Mo alloy containing ordered phase with Pt_2Mo-type structure at room temperature. *Mater. Sci. Eng. A* **2016**, *650*, 317–322. [CrossRef]
9. Yuan, L.; Hu, R.; Li, J.S. Evolution behavior of superlattice phase with Pt_2Mo-type structure in Ni-Cr-Mo alloy with low atomic Mo/Cr ratio. *J. Mater. Res.* **2016**, *31*, 427–434. [CrossRef]
10. Verma, A.; Singh, J.B.; Wanderka, N.; Chakravartty, J.K. Delineating the roles of Cr and Mo during ordering transformations in stoichiometric $Ni_2(Cr_{1-x}, Mo_x)$ alloys. *Acta Mater.* **2015**, *96*, 366–377. [CrossRef]
11. Gao, X.Y.; Hu, R.; Luo, G.L. The effect of Ti on precipitation of fully coherent $D0_{22}$ superlattice in an Ni-Cr-W-based superalloy. *Scr. Mater.* **2017**, *134*, 15–19. [CrossRef]
12. Chen, Y.; Hu, R.; Kou, H.C.; Zhang, T.B.; Li, J.S. Precipitation of nanosized $D0_{22}$ superlattice with high thermal stability in an Ni-Cr-W superalloy. *Scr. Mater.* **2014**, *76*, 49–52. [CrossRef]
13. Viswanathan, G.B.; Banerjee, R.; Singh, A.; Nag, S.; Tiley, J.; Fraser, H.L. Precipitation of ordered phases in metallic solid solutions: A synergistic clustering and ordering process. *Scr. Mater.* **2011**, *65*, 485–488. [CrossRef]
14. Hata, S.; Matsumura, S.; Kuwano, N.; Oki, K. Short range order and its transformation to long range order in Ni_4Mo. *Acta Mater.* **1998**, *46*, 881–892. [CrossRef]
15. Gao, X.Y.; Hu, R.; Yang, J.R. The effect of $Ni_3(Cr_{0.2}W_{0.4}Ti_{0.4})$ particles with $D0_{22}$ structure on the deformation mode and mechanical properties of the aged Ni-Cr-W-Ti alloy. *Scr. Mater.* **2018**, *153*, 44–48. [CrossRef]
16. Cai, S.S.; Li, X.W.; Tao, N.R. Orientation dependence of deformation twinning in Cu single crystals. *J. Mater. Sci. Technol.* **2018**, *34*, 1364–1370. [CrossRef]
17. Bhattacharjee, P.P.; Ray, R.K.; Tsuji, N. Cold rolling and recrystallization textures of a Ni-5 at.% W alloy. *Acta Mater.* **2009**, *57*, 2166–2179. [CrossRef]
18. Sarma, V.S.; Eickemeyer, J.; Schultz, L.; Holzapfel, B. Recrystallisation texture and magnetization behaviour of some FCC Ni-W alloys. *Scr. Mater.* **2004**, *50*, 953–957. [CrossRef]
19. Jakupi, P.; Noël, J.J.; Shoesmith, D.W. Intergranular corrosion resistance of sigma 3 grain boundaries in Alloy 22. *Electrochem. Solid State Lett.* **2010**, *13*, 3. [CrossRef]
20. Reed, B.W.; Kuma, M.; Minich, R.W.; Rudd, R.E. Fracture roughness scaling and its correlation with grain boundary network structure. *Acta Mater.* **2008**, *56*, 3278–3289. [CrossRef]
21. Shimada, M.; Kokawa, H.; Wang, Z.J.; Sato, Y.S.; Karibe, I. Optimization of grain boundary character distribution for intergranular corrosion resistant 304 stainless steel by twin-induced grain boundary engineering. *Acta Mater.* **2002**, *50*, 2331–2341. [CrossRef]
22. Sakaguchi, N.; Endo, M.; Watanabe, S.; Kinoshita, H.; Yamashita, S.; Kokawa, H. Radiation-induced segregation and corrosion behavior on $\Sigma3$ coincidence site lattice and random grain boundaries in proton-irradiated type-316L austenitic stainless steel. *J. Nucl. Mater.* **2013**, *434*, 65–71. [CrossRef]
23. He, W.J.; Hu, R.; Gao, X.Y.; Yang, J.R. Evolution of $\Sigma3^n$ CSL boundaries in Ni-Cr-Mo alloy during aging treatment. *Mater. Charact.* **2017**, *134*, 379–386. [CrossRef]
24. Gao, X.Y.; Hu, R.; Li, X.L.; Luo, G.L. Microstructure evolution during the precipitation and growth of fully coherent $D0_{22}$ superlattice in an Ni-Cr-W alloy. *Mater. Character.* **2016**, *118*, 244–251. [CrossRef]
25. Liu, Z.G.; Li, P.J.; Xiong, L.T.; Liu, T.Y.; He, L.J. High-temperature tensile deformation behavior and microstructure evolution of Ti55 titanium alloy. *Mater. Sci. Eng. A* **2017**, *680*, 259–269. [CrossRef]
26. Calcagnottok, M.; Ponge, D.; Demir, E.; Raabe, D. Orientation gradients and geometrically necessary dislocations in ultrafine grained dual phase steels studied by 2D and 3D EBSD. *Mater. Sci. Eng. A* **2010**, *527*, 2738–2746. [CrossRef]
27. Kubin, L.P.; Mortensen, A. Geometrically necessary dislocations and strain-gradient plasticity: A few critical issues. *Scr. Mater.* **2003**, *48*, 119–125. [CrossRef]
28. Jiang, M.G.; Xu, C.; Yan, H.; Fan, G.H.; Nakata, T.; Lao, C.S.; Chen, R.S.; Kamado, S.; Han, E.H.; Lu, B.H. Unveiling the formation of basal texture variations based on twinning and dynamic recrystallization in AZ31 magnesium alloy during extrusion. *Acta Mater.* **2018**, *157*, 53–71. [CrossRef]

29. Wang, J.A.; Liu, E.W.; Huang, H.C.; He, Y.L.; He, Y. Influence of rolling process on deformation and recrystallization texture of Ni-Cr-Mo alloy tape. *J. Mater. Eng. Perform.* **2020**, *29*, 811–818. [CrossRef]
30. Lu, Y.L.; Pike, L.M.; Brooks, C.R.; Liaw, P.K.; Klarstrom, D.L. Strengthening domains in a Ni-21Cr-17Mo alloy. *Scr. Mater.* **2007**, *56*, 121–124. [CrossRef]
31. Kumar, M.; Vasudevan, V.K. Mechanical properties and strengthening of a Ni-25Mo-8Cr alloy containing Ni_2(Mo, Cr) precipitates. *Acta Mater.* **1996**, *44*, 4865–4880. [CrossRef]
32. Onuki, Y.; Okayasu, K.; Fukutomi, H. Formation of {001} fiber texture in Fe-3mass% Si alloy during uniaxial compression deformation at elevated temperatures. *ISIJ Int.* **2011**, *51*, 1564–1565. [CrossRef]
33. Cohen, J.B.; Weertman, J. A dislocation model for twinning in f.c.c metals. *Acta Metall.* **1963**, *11*, 996–998. [CrossRef]
34. Davies, P. Grain-boundary plane reorientation in copper. *Philos. Mag. A* **1999**, *79*, 305–316.
35. Ponge, D.; Gottstein, G. Necklace formation during dynamic recrystallization: Mechanisms and impact on flow behavior. *Acta Mater.* **1998**, *46*, 69–80. [CrossRef]